Chapter V

Molecular dynamics simulations of pyronine 6G and rhodamine 6G dimers in aqueous solution

Rhodamine 6G and Pyronine 6G are the xanthene molecules which are well known for their remarkable photophysical properties. Therefore, they are frequently used as efficient laser dyes and fluorescent probes attached to molecules of biological interest.[103-108] However, aggregation of these dye molecules in aqueous solution [105,109] can interfere with their successful usage due to a drastic drop-off in the fluorescence quantum yield, discernible even at very low concentrations of $\sim 10^{-6}$ M. [110]

Self-aggregation of xanthene dyes poses a non-trivial physico-chemical problem because in general these molecules are positively charged, so that, on first glance, the interaction among such moieties is anticipated to be repulsive. Usually, aggregation in aqueous solution is observed for non-polar neutral molecules and ascribed to "hydrophobic interactions", [111] whereas recent molecular dynamics simulations on picrate anions in water revealed a definite trend for these charged moieties to form aggregates up to tetramers. [112] Thus, the atomistic mechanism of the latter type of aggregation remained controversial.

The association between ions of like charge could be caused by a number of possible physical mechanisms, ranging from direct bonding to simultaneous attachment to a third species. A special case of these interactions might be represented by π-stacking between flat, like-charged aromatic moieties. [113] The molecular mechanism of π-stacking, although directly observed in many organic and bioorganic systems, has not yet been fully theoretically rationalized, even for the case of neutral species. [114–116] Indeed, systematic theoretical studies on the π-stacking of like-charged aromatic residues are still rare. [109,112]

Hence, self-aggregation of xanthene dye molecules represents an interesting challenge for theoretical studies. Recently, Daré-Doyen *et al.* presented a molecular dynamics (MD) study on pyronine 6G (P6G) and rhodamine 6G (R6G) dimers in aqueous solution. [109] However, these MD simulations comprised rather short trajectories and some uncertainties remained regarding the force field description. In

particular, the atomic (partial) charges on the dye molecules do not seem to have been chosen according to standard procedures consistent with the force field used.

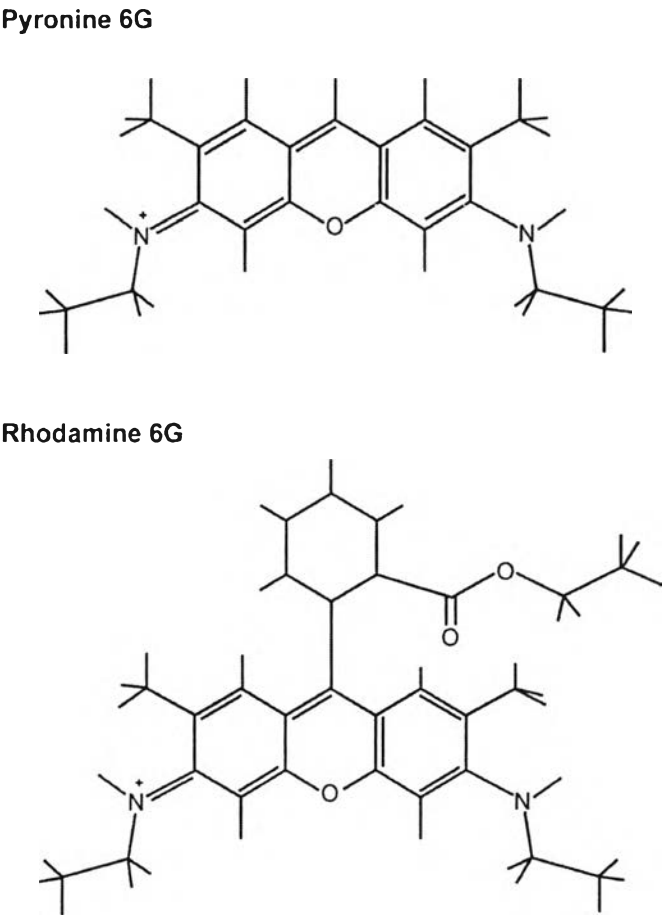

Figure 5.1 Structure of pyronine 6G (P6G) and rhodamine 6G (R6G).

These issues needed to be clarified before we were able to tackle MD simulations on the structure and relative mobility of rhodamine-DNA complexes. Therefore, we undertook a more detailed computational study to establish a suitable protocol for MD simulations of dimers of P6G and R6G (Figure 5.1) in aqueous solution. In the following, we will present and discuss these results and compare them to those of previous investigations. [109]

5.1 Atomic charges of pyronine 6G and rhodamine 6G

Pyronine 6G and Rhodamine 6G are not standard residues in the AMBER residue libraries, therefore, their force field parameters are not available. This and also a more recent variant of the AMBER force field [117] require partial atomic charges supplement when the program was used for the chromophores. The recommended procedure to generate atomic charges for AMBER 8 is based on a point-charge representation of the electrostatic potential (ESP) as obtained from a HF-SCF calculation with a 6-31G* basis set. [125] Strong local "variations" among atomic charges are controlled with a penalty function, applied in the "restrained" version (RESP) [118] of the Merz-Kollman EPS fitting procedure. [119] Unless mentioned otherwise, we based the determination of atomic charges on molecular geometries optimized at the B3LYP/6-31G* level.

All electronic structure calculations were carried out with the program package Gaussian98. [120] The results were summarized in Table 5.2 in comparison with those published by Daré-Doyen *et al.* [109] (in the following designated by "DD"). However, the calculated results were not reproduce the atomic net charges suggested by Daré-Doyen *et al.* when we checked the RESP atomic charges for both P6G and R6G, using a HF/6-31G* description (in the following referred to as "STD"), which is the recommended standard for supplementing the force field AMBER-95; [122] see Table 5.1

To clarify this discrepancy, we explored RESP atomic charges for P6G and R6G in more details. First, compared charge results obtained from HF-SCF calculations with basis sets of increasing flexibility, namely 6-31G, 6-31G*, 6-31G**, and 6-311G** were present. The results were given in Table 5.2 and Table 5.3 for P6G and R6G, respectively. On going from the 6-31G to the 6-31G* basis sets for P6G, *i.e.* by including polarization functions on non-hydrogen centers, the average absolute charges change by 0.03 *e*. By far the largest changes occur at the oxygen center O1 and its carbon neighbors C10, both charges decrease (by absolute value), *i.e.* for O1 from -0.439 *e* to -0.282 *e* and for C10 from 0.568 *e* to 0.426 *e*. Inclusion of polarization functions for hydrogen atoms (6-31G**) do not alter the charge distribution noticeably compared to the results yield from the recommended basis set (6-31G*), with an average absolute change of 0.004 *e*. The largest variation of an atomic charge was

found for the carbon centers C7 within the ethyl substituents of the nitrogen centers, namely 0.040 *e* and 0.028 *e* for 6-31G* and 6-31G**, respectively. Atomic partial charges vary somewhat more when the basis set was increased to triple-ζquality, 6-311G**, the average absolute change is 0.010 *e*. Determined RESP charges from a charge distribution generated at the B3LYP/6-31G* level was also studied; these charges are, in general, smaller by absolute value, *i.e.* the charge distribution appears to be locally less polarized than in the STD case (Table 5.2).

In addition, the net charge of the P6G geometry determined was derived at the HF/6-31G level. This method was proposed by Daré-Doyen *et al.*, [109] but the RESP charges are hardly affected if derived from charge distributions of the same level, B3LYP/6-31G* or HF/6-31G. At the electronic structure level used by Daré-Doyen *et al.*, [109] HF/6-31G for both structure and charge distribution, we also probed the differences between the RESP scheme [118] and the original ESP variant [119] as well as another version of potential-derived charges [121] (Table 5.2). However, with all these variations of the computational procedure, we were unable to reproduce the DD charges published in Ref. 109.

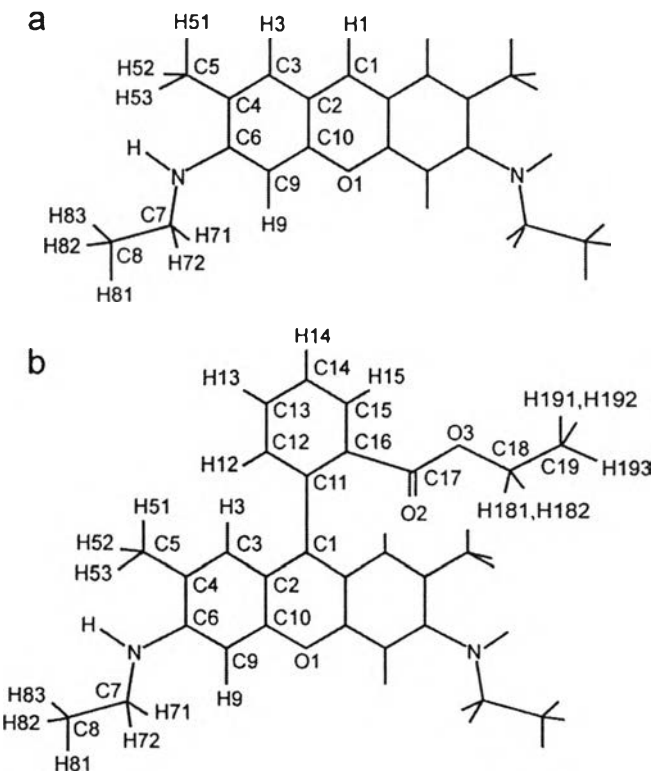

Figure 5.2 The atom labels for a) pyronine 6G (P6G) and b) rhodamine 6G (R6G).

Table 5.1 RESP charges (STD) of pyronine 6G and rhodamine 6G molecules obtained from single-point HF/6-31G* calculation on the B3LYP/6-31G* geometry (see Figure 5.2), where those value taken from Ref. 109 (DD) were also given for comparison.

	Pyronine 6G		Rhodamine 6G	
	DD	STD	DD	STD
C1	0.256	0.048	0.363	0.135
C2	-0.318	-0.118	-0.303	-0.104
C3	-0.211	-0.246	-0.237	-0.270
H3	0.218	0.206	0.213	0.213
C4	0.081	0.072	0.096	0.083
C5	-0.454	-0.286	-0.397	-0.299
H51-H53	0.152	0.101	0.129	0.101
C6	0.522	0.269	0.410	0.261
N	-0.742	-0.412	-0.608	-0.423
H	0.414	0.329	0.375	0.327
C7	0.382	0.040	0.271	0.062
H71-H72	-0.001	0.097	0.029	0.090
C8	-0.304	-0.315	-0.335	-0.319
H81-H83	0.086	0.107	0.099	0.105
C9	-0.680	-0.436	-0.550	-0.442
H9	0.251	0.182	0.205	0.181
C10	0.627	0.426	0.524	0.428
O1	-0.390	-0.282	-0.328	-0.287
H1 / C11	0.135	0.170	0.204	0.123
C12			-0.284	-0.194
H12			0.172	0.154
C13			-0.051	-0.114
H13			0.165	0.169
C14			-0.180	-0.115
H14			0.172	0.159
C15			-0.109	-0.146
H15			0.190	0.174
C16			-0.223	-0.161
C17			0.838	0.822
O2			-0.538	-0.568
O3			-0.561	-0.489
C18			0.381	0.383
H181-H182			0.005	-0.003
C19			-0.253	-0.293
H191-H193			0.070	0.087

Table 5.2 Comparison of various ESP derived charge distributions (in e) of pyronine 6G, based on the CHELPG approach,a the original Merz-Kollman procedure (MK),b and the MK procedure with restricted fitting (RESP).c The electrostatic potential was determined from HF-SCF or B3LYP calculations using various basis sets, for two optimized geometries HF/6-31G and B3LYP/6-31G*. The charges used in the preceding work of Daré-Doyen et al. (DD) are also shownd (see Figure 5.2 for the atomic labels).

Geometry		HF/6-31G			B3LYP/6-31G*			
ESP		CHELPG	MK	RESP	RESP			
Method	DD[d]	HF/6-31G	HF/6-31G	HF/6-31G	HF/6-31G	HF/6-31G*[e]	HF/6-31G**	HF/6-311G**
C1	0.256	0.082	0.183	0.072	0.078	0.048	0.040	0.053
H1	0.135	0.151	0.153	0.172	0.172	0.170	0.172	0.175
C2	-0.318	-0.165	-0.287	-0.164	-0.169	-0.118	-0.114	-0.137
C3	-0.211	-0.156	-0.186	-0.242	-0.235	-0.246	-0.243	-0.247
H3	0.218	0.176	0.202	0.210	0.210	0.206	0.206	0.210
C4	0.081	-0.132	-0.015	0.018	0.016	0.072	0.063	0.066
C5	-0.454	-0.078	-0.298	-0.235	-0.245	-0.286	-0.288	-0.289
H51-H53	0.152	0.053	0.111	0.094	0.096	0.101	0.104	0.105
C6	0.522	0.577	0.424	0.343	0.346	0.269	0.274	0.250
N	-0.742	-0.711	-0.532	-0.474	-0.475	-0.412	-0.406	-0.350
H	0.414	0.387	0.350	0.341	0.342	0.329	0.324	0.303
C7	0.382	0.359	0.182	0.039	0.034	0.040	0.028	0.013
H71, H72	-0.001	0.005	0.062	0.102	0.103	0.097	0.100	0.103
C8	-0.304	-0.307	-0.381	-0.295	-0.305	-0.315	-0.319	-0.308
H81-H83	0.086	0.092	0.117	0.103	0.106	0.107	0.110	0.107
C9	-0.680	-0.575	-0.589	-0.506	-0.508	-0.436	-0.438	-0.457
H9	0.251	0.219	0.219	0.200	0.202	0.182	0.183	0.186
C10	0.627	0.584	0.674	0.574	0.568	0.426	0.427	0.447
O1	-0.390	-0.482	-0.498	-0.451	-0.439	-0.282	-0.284	-0.283

[a] Ref. [136]. [b] Ref. [119]. [c] Ref. [118]. [d] Ref. [109]. [e] Standard charge distribution STD, used in the present work.

Table 5.3 Comparison of various ESP derived charge distributions (in *e*) of Rhodamine 6G, based on the MK procedure with restricted fitting (RESP). The electrostatic potential was determined using various basis sets, for two optimized geometries (HF/6-31G and B3LYP/6-31G*). The charges used in the preceding work of Daré-Doyen et al. (DD) are also shown. For the designation of the atomic centers, Figure 5.2.

Geometry		HF/6-31G	B3LYP/6-31G*				
	DD	HF/6-31G	HF/6-31G	HF/6-31G*	HF/6-31G**	HF/6-311G**	B3LYP/6-31G*
C1	0.363	0.098	0.092	0.135	0.121	0.113	0.073
C2	-0.303	-0.145	-0.138	-0.104	-0.103	-0.118	-0.026
C3	-0.237	-0.273	-0.275	-0.270	-0.265	-0.265	-0.288
H3	0.213	0.211	0.214	0.213	0.211	0.213	0.179
C4	0.096	0.037	0.041	0.083	0.073	0.075	0.176
C5	-0.397	-0.253	-0.260	-0.299	-0.301	-0.305	-0.320
H51-H53	0.129	0.095	0.097	0.101	0.103	0.106	0.106
C6	0.410	0.337	0.332	0.261	0.266	0.244	0.080
N	-0.608	-0.483	-0.487	-0.423	-0.417	-0.360	-0.283
H	0.375	0.338	0.340	0.327	0.323	0.301	0.284
C7	0.271	0.054	0.055	0.062	0.049	0.034	0.028
H71-H72	0.029	0.096	0.096	0.090	0.093	0.096	0.091
C8	-0.335	-0.293	-0.309	-0.319	-0.324	-0.314	-0.305
H81-H83	0.099	0.100	0.104	0.105	0.108	0.105	0.104
C9	-0.550	-0.519	-0.513	-0.442	-0.445	-0.468	-0.286
H9	0.205	0.201	0.201	0.181	0.182	0.187	0.141
C10	0.524	0.587	0.573	0.428	0.432	0.452	0.311
O1	-0.328	-0.461	-0.447	-0.287	-0.291	-0.289	-0.231
C11	0.204	0.317	0.306	0.123	0.143	0.154	0.112
C12	-0.284	-0.260	-0.263	-0.194	-0.203	-0.198	-0.156
H12	0.172	0.163	0.165	0.154	0.156	0.154	0.126
C13	-0.051	-0.092	-0.088	-0.114	-0.111	-0.119	-0.105
H13	0.165	0.168	0.169	0.169	0.168	0.174	0.144
C14	-0.180	-0.142	-0.145	-0.115	-0.117	-0.125	-0.088
H14	0.172	0.161	0.163	0.159	0.158	0.164	0.135
C15	-0.109	-0.072	-0.074	-0.146	-0.145	-0.148	-0.116
H15	0.190	0.159	0.163	0.174	0.173	0.176	0.137
C16	-0.223	-0.367	-0.359	-0.161	-0.165	-0.178	-0.147
C17	0.838	1.088	1.077	0.822	0.815	0.839	0.680
O2	-0.538	-0.680	-0.669	-0.568	-0.566	-0.569	-0.487
O3	-0.561	-0.628	-0.622	-0.489	-0.480	-0.488	-0.397
C18	0.381	0.400	0.415	0.383	0.356	0.368	0.327
H181-H181	0.005	0.010	0.004	-0.003	0.005	0.001	0.003
C19	-0.253	-0.278	-0.303	-0.293	-0.298	-0.292	-0.285
H191-H193	0.070	0.086	0.091	0.087	0.090	0.088	0.088

Changes of the R6G atomic charges as a function of the method used are the same fashion as those of P6G. The oxygen partial charges increase when the polarization functions were taken into account. Along with this, the neighboring carbon charges decrease when using 6-31G instead of 6-31G* basis set (STD). The average absolute charges change by 0.04 *e*. Including polarization function for hydrogen (6-31G**) does not alter the charge distributions noticeably, as compared to the 6-31G* results. The maximum atomic charge difference is found for C18 (see Figure 5.2) within the xanthene ring in rhodamine 6G; 0.383 *e* and 0.365 *e* for 6-31G* and 6-31G**, respectively (see Table 5.3). There was no significant change in the atomic partial charges even when using triple-ζ basis set 6-311G**. The positive and negative charges calculated with the B3LYP/6-31G* method are, as a rule, possessed of lower absolute values, as compared with the those from the basis set HF/6-31G*. Moreover, atomic partial charges were calculated for two different rhodamine structures, geometry-optimized with HF/6-31 and B3LYP/6-31G* basis sets. These results showed that the structure alterations do not significantly change the atomic partial charge values thus obtained.

Taking into account all the results describing above, charges derived from the HF/6-31G* (Table 5.1) were used for the MD simulation, since this is the default approach applied in the AMBER force field to calculate partial charges on atoms.

As the STD and DD solutions of the problem of electrostatics differed significantly, the resulting electrostatic model potentials $V_{STD}(r)$ and $V_{DD}(r)$ via their relative difference R(r) was decided to study as defined at

$$R(r) = \Delta V(r)/\overline{V}(r) = (V_{DD}(r) - V_{STD}(r)) / [(V_{DD}(r) + V_{STD}(r))/2]. \qquad (5.1)$$

where the potential at each point of the probe plane is calculated by

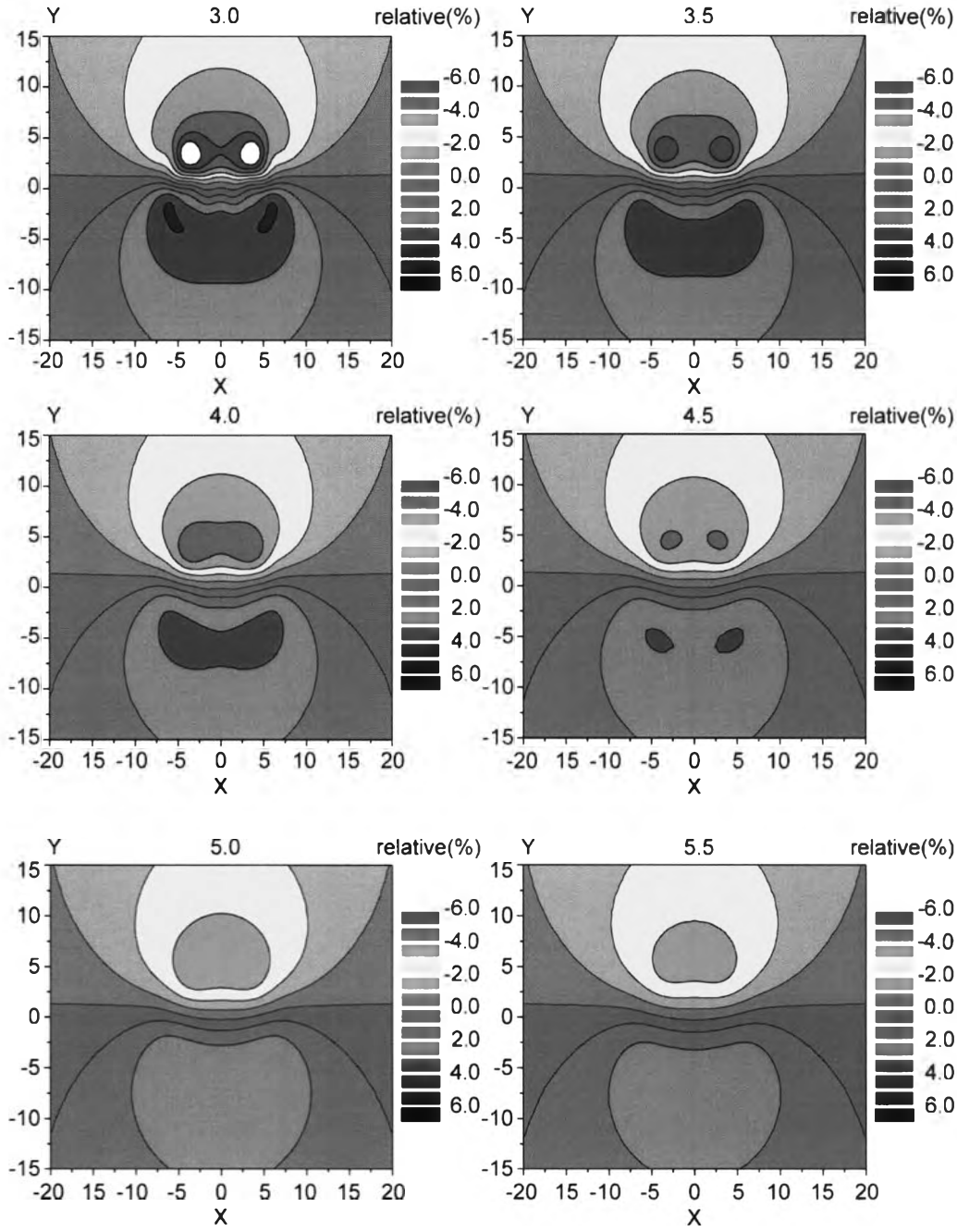

Figure 5.3 Relative R(r) quantities (%) of the potential yielded from the between DD and STD charges.

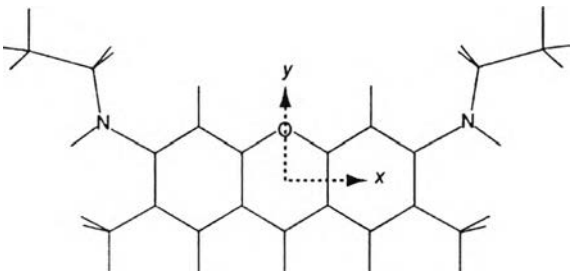

Figure 5.4 The xantylium plane of P6G lies on the *xy*-plane and the origin is at the midpoint O and the opposite C.

$$V_{DD}(r) = \sum_i \frac{q_i(DD)}{|r - r_i|}) \tag{5.2}$$

$$V_{STD}(r) = \sum_i \frac{q_i(STD)}{|r - r_i|}) \tag{5.3}$$

with

$$\Delta V(r) = V_{DD}(r) - V_{STD}(r) \tag{5.4}$$

$$\overline{V}(r) = \tfrac{1}{2}(V_{DD}(r) + V_{STD}(r)) \tag{5.5}$$

Center of the coordinated was located at the center of the O and opposite C (Figure 5.4). The results were given in Figure 5.3. The results show that the maximum values of the *R(r)* in the molecular plane decrease from 6–7% and to 3–4% at the distance of 3.5 Å and 5.5 Å, respectively.

As another direct comparison, the electrostatic potential energy curves during the relative rotation of the monomers in P6G dimer were examined. That interaction features a double minimum shape, again with small but distinct differences (Figure 5.5). At an inter-planar separation of 3.8 Å, the two minima are located at torsion angles β (Figure 5.8) of ~90° and ~270°, but these angles differ by about 10° between the two sets of charges. Also the barriers at 0° twist, ~5 kcal/mol, differ by ~10%. Although these differences between the two representations of the electrostatic interaction may seem small, they can significantly affect the dynamics of the dimers at

longer times. Note that the minima of the electrostatic interaction at twist angles of ~90° and ~270° indicate a dominant role of the quadrupole over the dipole term.

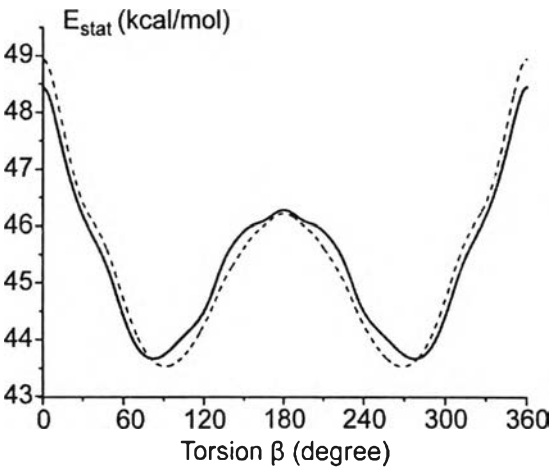

Figure 5.5 Electrostatic interaction between the two monomers of a P6G model dimer as a function of the torsion angle β (see Figure 5.8), relative to eclipsed stacking β = 0°. Both xantylium planes are parallel at a distance of 3.8 Å. Calculations for the atomic charge assignments STD and DD, solid and dashed lines, respectively.

In addition, the interaction between water molecule and P6G was also investigated. The calculations were performed by Sander module in AMBER. The optimized water molecule was probed on the plane which the distance at 2.5 and 3 Å (see Figure 5.6)

Figure 5.7 shows the binding energy surface of water and P6G complex. The STD charges were selected for P6G molecule and were carried out by AMBER program. There are attractive and repulsive interactions between theses molecules. The repulsive interaction shows when the water molecule is close to O or N atom of P6G. The interaction between water and P6G is about -5.22 kcal/mol when the coordinate of oxygen of water molecule is at the (-6.5, 1, 2.5).

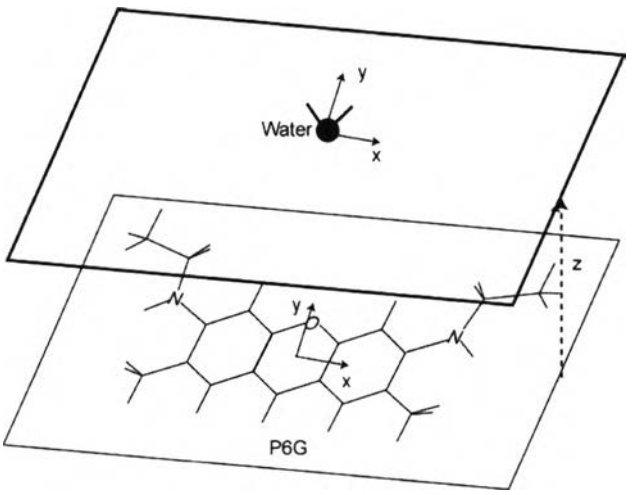

Figure 5.6 The probed water plane and the P6G molecules are on *xy* plane and *z* is the distance between O of water molecule and P6G.

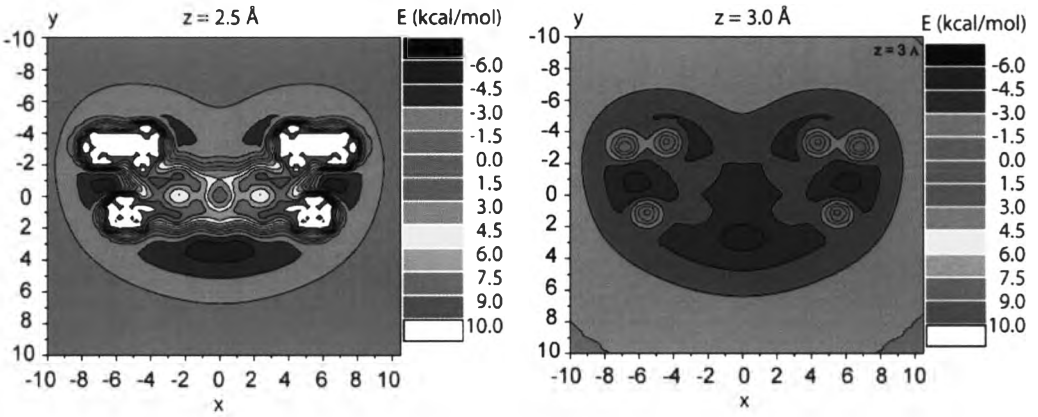

Figure 5.7 Biding energy surface between P6G and a water molecule using AMBER program.

Moreover, the same configuration as obtained in AMBER was used for MP2 and HF calculations. The binding energies of water and P6G are -5.22, -7.76 and -5.09 kcal/mol, for AMBER, MP2/6-31g** and HF/6-31g**, respectively. The result from force filed calculation agrees well with ab *initio* method (see Table 5.4).

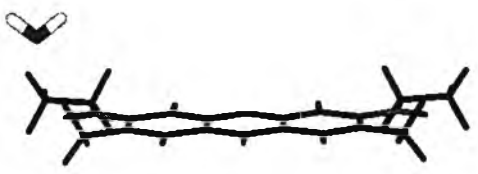

Table 5.4 The binding energy of P6G and a water molecule where the coordinate of O of water is (-6.5, 1, 2.5).

	ΔE (kcal/mol)
AMBER	-5.22
MP2/6-31g**	-7.76
HF/6-31g**	-5.09

5.2 Models and methods

MD simulations were carried out using the program suite AMBER 8. [122] For continuity with previous MD simulations on DNA duplexes,[123,124] the force field AMBER-95 was selected.[125] All MD simulations were performed for dye molecules in aqueous solution using Sander module. For this purpose, we inserted each system into a rectangular box containing TIP3P water molecules [126] and applied periodic boundary conditions. Table 5.5 shows the dimensions of the boxes and the numbers of water molecules for the various solutes. To compensate the positive charge of each chromophore and to render the whole system neutral, we added a chloride ion per dye molecule to each box.

We followed the usual procedures to establish initial structures of MD runs. We first obtained equilibrium geometries [122,127,128] and then we generated the dynamics, invoking the SHAKE algorithm for bonds involving H atoms. [129,130] Specifically, we started each simulation with a minimization of the total energy by applying a conjugate gradient optimization to the solvent structure. Then we carried out a series of equilibration MD runs on the water structure at pressure P = 1 atm while we kept the structure of the solute fixed. Over 20 ps, the system was gradually heated to 300 K and then was maintained at that temperature for 80 ps; here, as in all MD runs, the time steps were 2 fs. Afterwards, MD production runs were performed for at

least 2.5 ns, using an NPT ensemble with temperature T = 298 K and pressure P = 1 atm. For each system under study, we analyzed the MD trajectories in two time ranges, based on structure snapshots taken at each picosecond. To compare with the simulations of Daré-Doyen *et al.*,[109] we treated the first 700 ps of a production trajectory separately. Then we extended the MD trajectory by 800 ps without analysis. Finally, we analyzed the MD trajectory from 1.5 to 2.5 ns.

Table 5.5 Parameters of MD simulations: numbers of water molecules *N* in the unit cell and dimensions of the unit cell (in Å) after equilibration.

		N	Dimension
P6G monomer	PME	1174	37 × 35 × 28
P6G dimer	PME	1275	36 × 36 × 29
	cutoff	1275	35 × 35 × 28
	PME, TI[a]	1530	39 × 39 × 31
R6G monomer	PME	1450	36 × 36 × 33
R6G dimer	PME	1805	40 × 36 × 40

[a] Used for thermodynamic integration.

5.2.1 Molecular dynamic simulations of pyronine 6G

MD simulations of P6G dimers with the monomers (in the geometry optimized at the B3LYP/6-31G* level) was started at oriented in anti-parallel fashion (Figure 5.8), eclipsed at an inter-plane separation of 3.8 Å.

In view of these methodological issues, MD calculations for P6G and its dimers were carried out for two set of charges (STD and DD), to study structural and dynamic affects of these force field parameters in a consistent fashion. The results were checked the consequences.

The different treatments of the electrostatic interaction were applied for simulations. As a standard, we used the particle mesh Ewald (PME) technique [131] with the default parameters as implemented in AMBER 8. [122] Daré-Doyen *et al.*, [109] after some test calculations, had opted for the residue-based cutoff procedure

implemented in older versions of AMBER. Thereby, if any pair of atoms of two "residues" (molecular moieties) was inside the cutoff, the nonbonding and electrostatic interactions between all atom pairs of these two residues were included. From version 6 on, AMBER switched to an atom-based interpretation of the cutoff and a PME treatment of the electrostatic interactions as standard. [132,136]

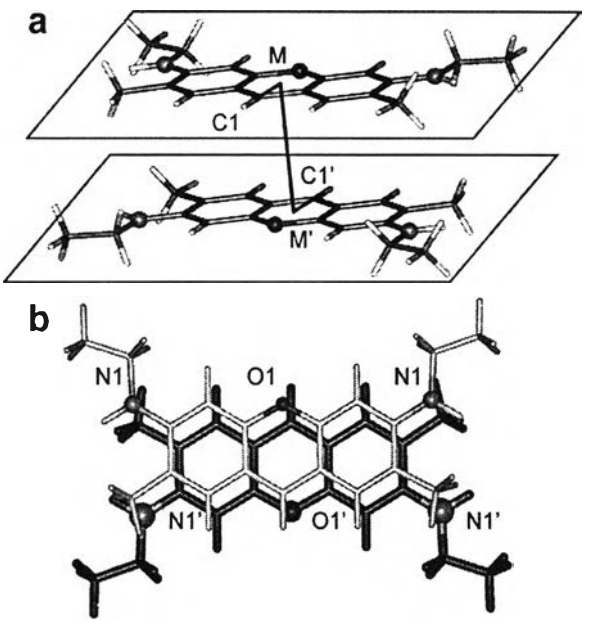

Figure 5.8 a) Torsion angle β = C1-M-M'-C1' and *M-M* distance *M–M'*, defined for the P6G dimer: M is the center of mass of the 14 heavy atoms in xanthylium rings which make up the three aromatic rings. b) P6G dimer in which monomer1 (light and thin) is above monomer2 (dark and thick) in antiparallel configuration, $\beta = 180°$.

Furthermore, for each of these two force field variants, MD trajectories with and without invoking the PME technique were generated. In calculations with Ewald summation, we applied a cutoff of 10 Å to the van der Waals interactions, but like Daré-Doyen *et al.* [109] we used an overall cutoff of 12 Å (nonbonding and Coulomb interactions) in calculations which invoked a residue-based selection of the electrostatic interaction. In this way, the electrostatic interaction between the two monomers of a xantene dimer was always accounted in full. These latter calculations were carried out with the module Sander_Classic of AMBER 6.[122]

To obtain the free energy profile for the interaction of two P6G units at varying distance, this is invoked thermodynamic integration. [133] For this purpose, we resorted to the module GIBBS of AMBER 6. [122] The holonomic distance constraints [134] via the non-interacting centroids of the two monomers was defined (Figure 5.9). The constrained distance was changed in steps of 0.25 Å from 2.5 Å to 4.0 Å and then in steps of 0.5 Å up to a maximum of 12 Å which were considered in 24 cases. In each cases, after an equilibration phase of 20 ps, the data was collected for 180 ps at each ps. These simulations were carried out under the same conditions applied previously (NPT ensemble, PME treatment of electrostatic interactions), except time steps of 1 fs were used. Solute and solvent were separately coupled to a heat bath with the Berendsen algorithm. [135]

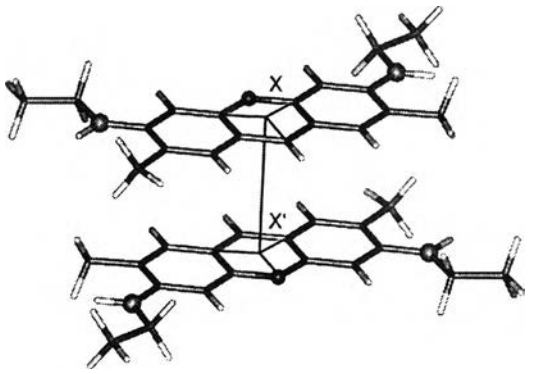

Figure 5.9 Constrained distance *X*-*X'* between the centroids *X*, *X'* of the central rings of the xantylium moieties.

5.2.2 Molecular dynamic simulations of rhodamine monomers at of 10 Å separation

The simulations were performed in aqueous solution using STD charge of R6G. In this simulation, the monomers were initially separated by 10 Å with β = 180°. The calculation was studied using AMBER8 and the PME technique [132,136] with the default parameters as implemented. The cutoff was 10 Å. The idea is to examine how the dimer can be formed for the positively charge molecules.

5.2.3 Molecular dynamic simulations of rhodamine 6G dimer

For the R6G dimer, we used a starting geometries (Figure 5.10): an anti-parallel configuration (β = 180°) in full analogy to the P6G dimer at an inter-plane separation of 3.8 Å. In addition, the used atomic partial charged was only STD set and the simulation was performed using PME technique with 10 Å cutoff.

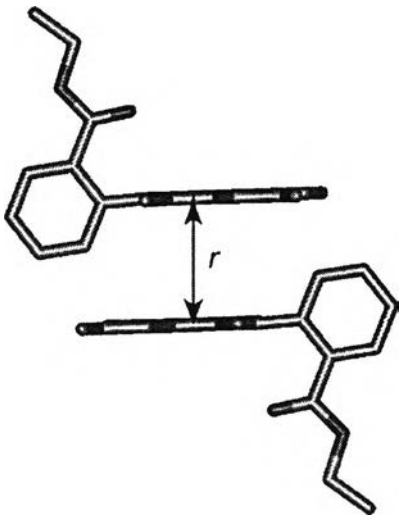

Figure 5.10 Orientation of the R6G dimers in the antiparallel configuration, β = 180° with the separation *r*.

5.3 Molecular dynamics results

5.3.1 Pyronine 6G dimers

Four defined variables to quantify the structure of a dimer were used. The definition of these parameters starts with two pertinent characteristics, namely the average plane P from 14 atoms in each xantylium group and its center of mass M (see Figure 5.8). Then four key structure parameters of a dimer are (*i*) the distance *M-M* between the two centers of mass M and M' of each xantylium group, (*ii*) the average *M-P* of the two distance *M-P'* and *M'-P* between the center of mass M of one xantylium system to the plane P' of the second xantylium system of a dimer and *vice versa*, and (*iii*) the roll angle α between the two xantylium planes P and P', and *(iv)* the torsion angle β, *i.e.* the dihedral angle C1-M-M'-C1' (see Figure 5.8 and Figure 5.10).

Daré-Doyen *et al.* used a different dihedral angle, C1-M-C1'-M' which they also called β; [109] to avoid confusion, we refer to that dihedral angle as β'. The anti-parallel reference configuration of a dimer is characterized by $\beta = 180°$ and $\beta' = 0°$. For the dominant range of inter-plane distances, the torsion angles β and β' essentially complement each other to 180° within a few degrees.

Discussions of the MD results were started by analyzing structure and dynamics of a P6G dimer because the carbethoxyphenyl substituent of R6G is complicated matters for such a dimer, Figure 5.1. Table 5.6 summarizes the main structural findings from our MD simulations. Starting with the most accurate results, obtained by averaging data generated with the PME approach for the "long time" interval from 1.5 to 2.5 ns, we note that the *M-M* distances for the force field variants STD, (4.25±0.53) Å, and DD, (4.16±0.54) Å, are compatible. As expected for geometric reasons, the corresponding average *M-P* distances are shorter, (3.44±0.21) Å and (3.46±0.21) Å, respectively (Table 5.6). These latter distances between the planes of π–stacks are quite comparable to literature data.[114–116] The xantylium planes stay parallel to each other, with an average roll angle α of (11±7) ° for STD and (10±7)° for DD parameters. Also the torsion angles β, (55±33)° for STD and (56±34)° for DD, compare well for both variants of the force field (Table 5.6). The torsion angles β vary over a rather wide range, with standard deviations (SD) of ~30°, but the average configuration is closer to a parallel arrangement of the xantylium groups than to an anti-parallel configuration (see below). As expected, the alternative torsion angle β' is essentially the complement of β to 180°. At long times, both force field variants, STD and DD, yield essentially the same standard deviations for each of these structure parameters.

Next, we compare the results of Table 5.6 according to three criteria that reflect on alternative MD strategies. [109] First, we address the effect of using a residue-based cutoff of 12 Å for the Coulomb interaction, based on the more accurate long-time averages (1.5–2.5 ns). For each set of charges, STD and DD, the long-time average values of all four structural parameters, *M-M*, *M-P*, α, and β, from the trajectory obtained with Coulomb cutoff are compatible with the corresponding averages obtained with the PME treatment (Table 5.6). For both STD and DD results, there is a trend to smaller SD values of all characteristics shown in Table 5.6 (with the

exception of *M-M* for DD charges), on going from PME results to those obtained with a Coulomb cutoff. Still, according to these long-time results, we can confirm the conclusion [109] that for the present systems the PME method and the residue-based cutoff of the Coulomb interaction yield results which are comparable to a large degree.

Table 5.6 Geometric parametersa of a pyronine 6G dimer, averaged over various time intervals of MD trajectories. Results are shown for various force field variants (STD, DD) and two treatments of the electrostatic interaction, particle mesh Ewald technique (PME) and a residue-based cutoff of 12 Å.

		1–700 ps					1501–2500 ps			
Charges		STD[b]		DD[c]		DD/PW[d]	STD[b]		DD[c]	
M-M, Å	PME	4.08	±0.52	4.17	±0.59		4.25	±0.53	4.16	±0.54
	cutoff	4.21	±0.58	4.36	±0.47	4.14±0.52	4.24	±0.43	4.19	±0.57
M-P, Å	PME	3.40	±0.20	3.50	±0.21		3.44	±0.21	3.46	±0.21
	cutoff	3.45	±0.25	3.54	±0.20	3.43±0.25	3.48	±0.16	3.46	±0.20
Roll α, °	PME	12	±8	10	±9		11	±7	10	±7
	cutoff	12	±10	12	±10	9±18	9	±5	9	±6
Torsion β, °	PME	95	±40	109	±57		55	±33	56	±34
	cutoff	141	±37	161	±16		37	±19	47	±26
Torsion β', °	PME	89	±36	70	±56		124	±30	123	±31
	cutoff	41	±37	19	±17	4±18	139	±19	130	±26

[a] See Figure 5.8 for the definitions. [b] Standard force field, present work. [c] Atomic partial charge from Ref. 109, present work. [d] Previous work, Ref. 109.

This brings us to our second comparison, namely long-time (1501–2500 ps) vs. short-time (1–700 ps) trajectory averages (Table 5.6). The corresponding averages and standard deviations of the distances *M-M* and *M-P* as well as of the roll angle α are essentially compatible between all MD set-ups (STD vs. DD, PME vs. cutoff). However, long-time and short-time results for the torsion angle β (and its complement β') are noticeably different.

At short times, PME results for both variants of the force field, STD and DD, exhibit a propensity to larger values of the torsion angle β (Figure 5.12), (95±40)° instead vs. (55±33)° and (109±57)° vs. (56±34)°, respectively. In particular, the SD values are significantly larger at shorter times (PME: 40°, 57° vs. 33°, 34°;

Table 5.6). In fact, as these MD trajectories had been started in anti-parallel configuration, $\beta = 180°$, following the suggestion of earlier work, [109] they take some time to reach smaller torsion angles. This effect is particularly noticeable for trajectories generated with Coulomb cutoff where large values of β dominate for the first 500–600 ps (Figure 5.12). This analysis confirms that short simulation times of at most 700 ps, as adopted in Ref. 109, are not adequate for sampling the phase space. The subsequent discussion of physical aspects will be based only on structural parameters that have been averaged over later times, from 1.5 to 2.5 ns.

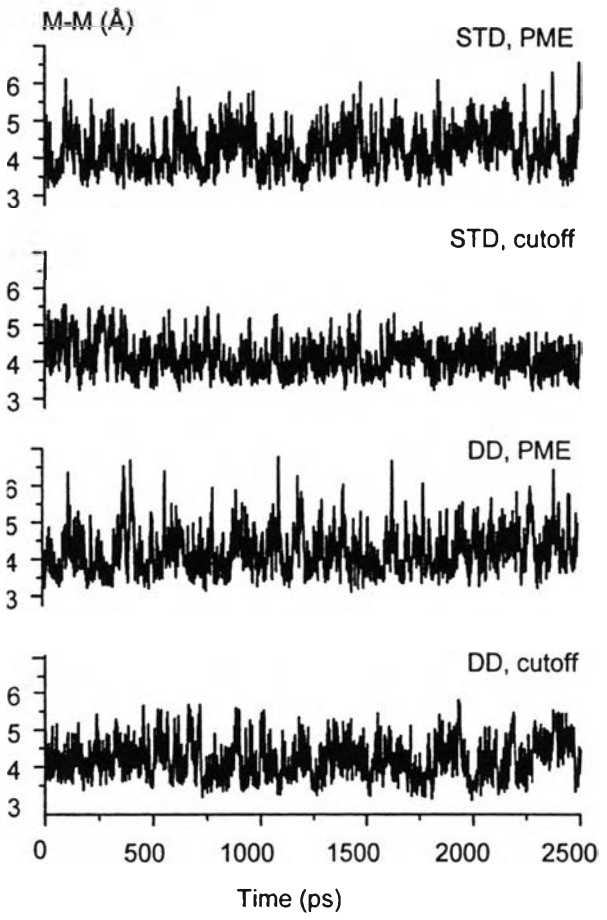

Figure 5.11 *M-M* distance (see Figure 5.8) in pyronine 6G dimers based on various MD protocols. Simulations treating the Coulomb interaction with a PME technique and a residue-based cutoff of 12 Å, for force field variants with standard (STD) or DD charge assignment (see text).

Based on the long-time averages, we turn to the differences caused by the force field variants STD and DD as third aspect of the comparison. Above we noted some differences in the structural parameters between both the two sets of partial atomic charges when a Coulomb cutoff was employed (Table 5.6). However, with the PME approach, both sets of charges yield very similar results. Still, the STD charges are preferable for consistency with the AMBER protocol of charge assignment. [125]

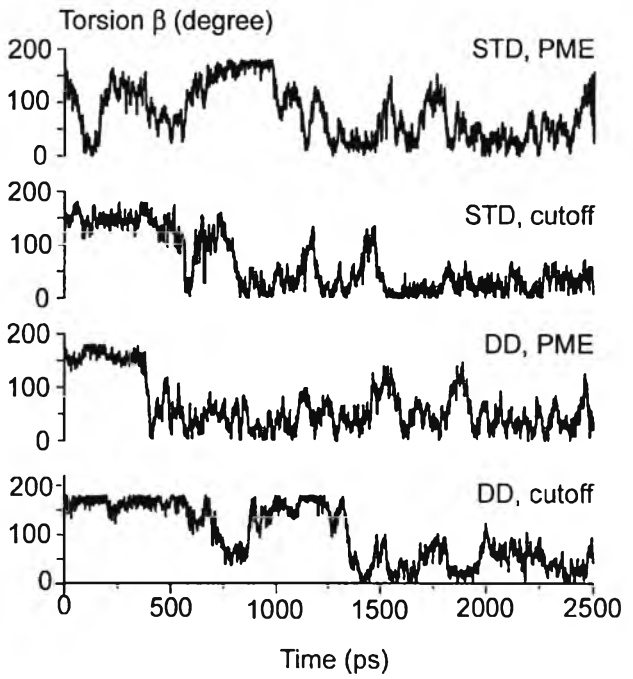

Figure 5.12 Torsion angle *β* (see Figure 5.8) of P6G dimers based on various MD protocols. Simulations treating the Coulomb interaction with a PME technique and a residue-based cutoff of 12 Å, for force field variants with standard (STD) or DD charge assignment (see text).

Summarizing our methodological study, we decided to base our interpretation of *physical* properties of xanthene dimers in aqueous solution on MD simulations (*i*) obtained with the RESP-based charge assignment STD, (*ii*) employing the PME technique for an accurate representation of the Coulomb interactions, and (*iii*) using only data from later sections of trajectories, beyond 1 ns (Figure 5.11, Figure 5.12). In contrast, the previously suggested physical picture, results DD/PW of Table 5.6, [109] were gleaned from a short trajectory (up to 700 ps), generated with a Coulomb cutoff. Based on the pertinent structural parameters of Table 5.6, our present

results suggest a very similar picture for P6G dimers as discussed previously [109] – with one notable exception. DD/PW results [109] and long-time STD/PME averages of the present work for the torsion angle β' do not agree at all (Table 5.6). Whereas previously an antiparallel orientation of the two monomers had been diagnosed, $\beta' = (4\pm18)°$, our best results indicate rather large values for the alternative torsion angle, $\beta' = (124\pm30)°$, which in addition fluctuates over a wider range.

5.3.2 Rhodamine 6G

The simulations of R6G ware performed using only STD atomic charge with PME technique. Before the other calculations on R6G were studied. Test calculations were investigated on Rhodamine 6G monomer (see Figure 5.2). The behavior of the system total energy along the MD trajectory is shown Figure 5.13. Time of the production run is 1 ns. The RMSD of the total energy is 0.2 kcal/mol.

Table 5.7 lists most important bond lengths in Rhodamine 6G calculated with B3LYP/6-31G* and derived from MD trajectory by averaging. The parameters are slightly different. The most considerable difference is found for bond distance C1-C11 between the phenyl ring and the xanthene moiety in Rhodamine 6G (See Figure 5.2). The average bond distance of C1-C11 is 1.410 Å with variance of about 0.023 Å, while in the DFT optimized structure it is equal to 1.471 Å. Moreover, the average distances N-C6 and N– C7 of 1.406 ± 0.030 Å and 1.484 ± 0.037Å, are shorter by 0.048 and 0.040 Å, respectively than in the DFT optimized structure. The average bond lengths N'-C6' and N'–C7' are also somewhat shorter by 0.048 and 0.041Å, respectively.

The dihedral angle C2-C1-C11-C16 is flexible and deviates from the optimized value (See Figure 5.14). Alternate the changed of the dihedral, it angle goes up from 80◦ to 130 ◦, and goes down from 80° to 40°, as shown in Figure 5.14a. Moreover, Figure 5.14b shows the histograms of the C2-C1-C11-C16 dihedral angle. It indicated that the dihedral angle is frequently found at 70° ± 9° and 108° ± 9°, while the optimized structure is 87.1°. However, the spectroscopic properties are slightly different from the optimized structure. The wave lengths obtained from the AM1 calculation are shifted by 2.1 and 3.7 nm for C2-C1-C11-C16 dihedral angle at 70° and

87 °, respectively. The lowest state spectra at AM1 are 459.7, 457.6 and 461.3 nm for dihedral angle at 70°, 87 ° and 110°, respectively. It should be noted that for the RMSD calculations the whole structure can be divided into two Fragments. The xanthene part is the Fragment 1 and the carbethoxyphenyl is the Fragment 2 shown in Figure 4.3.

Table 5.7 Comparison of selected bond lengths in xantylium of Rhodamin6G, in Å

Parameter	B3LYP/6-31G*	average bond distance	Δ
O1-C10	1.379	1.375 ± 0.028	0.004
O1-C10′	1.380	1.375 ± 0.030	0.005
C1-C2	1.408	1.419 ± 0.021	-0.011
C2-C10	1.424	1.405 ± 0.022	0.019
C10-C9	1.390	1.393 ± 0.022	-0.003
C9-C6	1.420	1.393 ± 0.023	0.027
C6-C4	1.454	1.403 ± 0.023	0.051
C4-C3	1.370	1.404 ± 0.025	-0.034
C3-C2	1.425	1.411 ± 0.024	0.014
C6-N	1.358	1.406 ± 0.030	-0.048
N-C7	1.444	1.484 ± 0.037	-0.040
C1-C11	1.471	1.410 ± 0.023	0.061
C9′-C10′	1.390	1.389 ± 0.025	0.001
C10′-C2′	1.424	1.406 ± 0.023	0.018
C2′-C3′	1.425	1.412 ± 0.025	0.013
C3′-C4′	1.370	1.402 ± 0.026	-0.032
C4′-C6′	1.454	1.406 ± 0.020	0.048
C6′-N′	1.358	1.406 ± 0.026	-0.048
N′-C7′	1.444	1.485 ± 0.027	-0.041
C2′-C1′	1.408	1.417 ± 0.023	-0.009

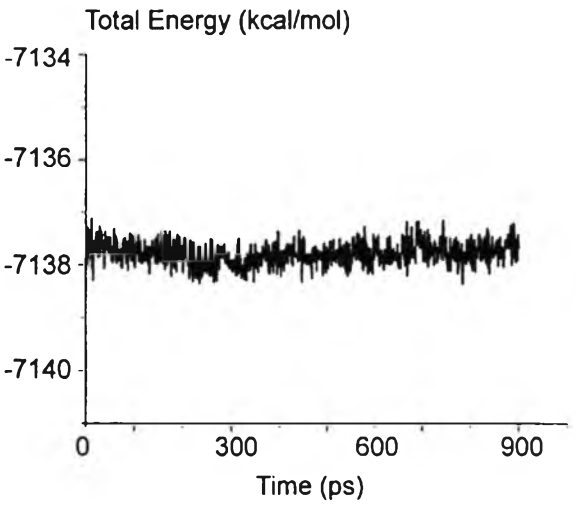

Figure 5.13 Total energy along the MD trajectory for R6G in water.

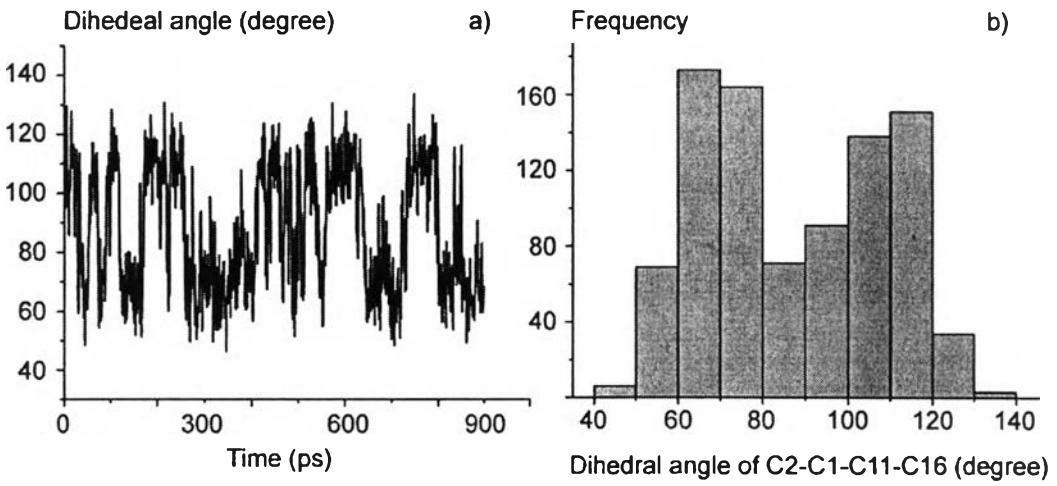

Figure 5.14 Fluctuation of the dihedral angle C2-C1-C11-C16 in R6G along the MD trajectory (a) and its distribution (b).

The stability of each trajectory was evaluated in terms of RMSD. Snapshots were extracted from the MD trajectory at each ps and compared to the initial structure. Plots of the RMSD values as a function of time are shown in Figure 5.15. In the first measure, the deviation of Fragment 1 was calculated. The average RMSD is 0.61±0.11 Å. The RMSD reached a value of about 0.93 Å because of the flexibility of two the end methyl groups (C8 and C8′ in Figure 5.2). In the second measure, the RMSD was calculated on Fragment 2. The structure deviated by about 0.14 Å until 50 ps, then the

RMSD increased to 0.64 Å. It was interesting to explore the flexibility of this fragment. The RMSD calculated for all heavy atoms, excluding C19, is 0.12±0.03 Å (Figure 5.15). Figure 5.16 demonstrates the flexibility of Fragment 2. The RMSD value calculated for two snapshots is 0.60 Å (Figure 5.16b). Smaller RMSD value is shown in Figure 5.16a).

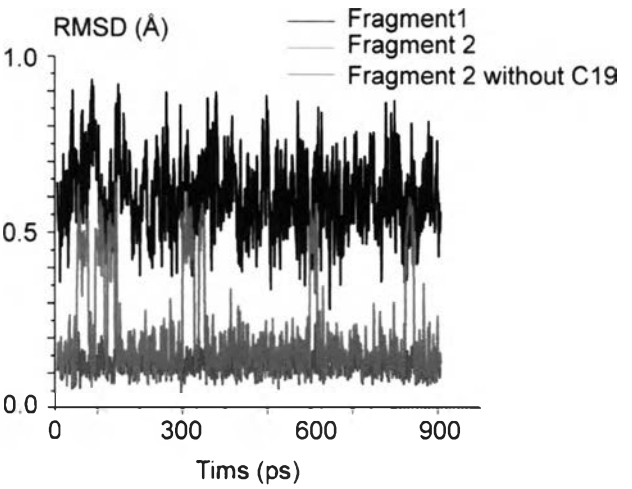

Figure 5.15 RMSD derived from 900 ps MD trajectory of Fragment 1 (black), Fragment 2 (green) and Fragment 2 without C19 (red) relative to initial structure.

Figure 5.16 Comparison of MD snapshots (blue) with the initial structure (red) for Fragment 2: two snapshots at 592 ps. (a) and 593 ps. (b) are presented.

5.3.2.1 Rhodamine monomers at the separation 10 Å

Figure 5.17 presents the results of an MD simulation on a R6G dimer where the trajectory has been started with the two monomers separated at 10 Å. Within 150–200 ps, both characteristic distances *M-M* and *M-P* quickly reduce to their typical range of 4–5 Å and 3–4 Å, respectively, and a solvated dimer of two positively charge R6G monomer is formed. The plot shows clearly that the dimer was formed after ~250 ps., where the *M-M* distance is in equilibrium, *i.e.*, solvent effect was found to play strong role to facilitated the dimer formation between the two highly positive charges.

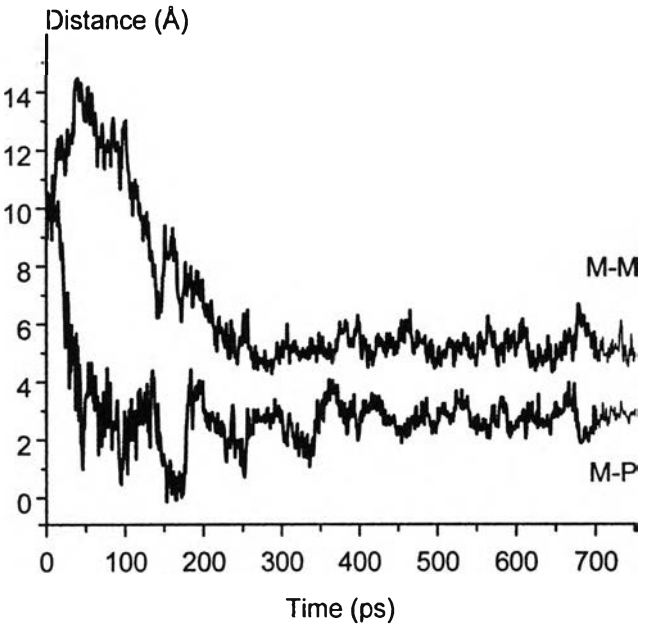

Figure 5.17 Changes of the *M-M* and *M-P* distances of a R6G dimer yielded from an MD run starting in an anti-parallel configuration at an inter-plane separation of 10 Å.

Figure 5.18 shows another possible dimer configuration formed in solvent. The monomers were turned during the simulation and two carbethoxyphenyl groups pointed out in the same direction, which obstructs the dimer to change into the antiparallel configuration (Figure 5.10). This conformation prevents the two monomers to approach closer than 4 Å. The simulation might be investigated in longer time scale until the global minimum structure will be reached. Since our interest for this investigation is to examine the dimer formation. This was already detected within the first 200 ps, therefore, we decided to stop the simulation at 800 ps.

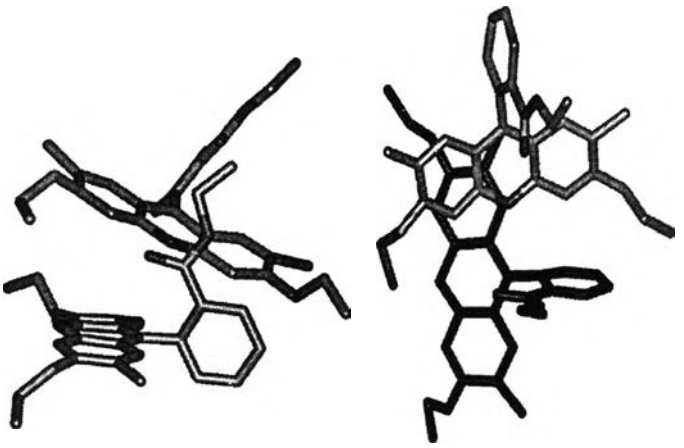

Figure 5.18 Side and top views of R6G snapshot taken from simulation started with an anti-parallel configuration at an inter-plane separation of 10 Å.

5.3.2.2 Rhodamine 6G dimer

Now we turn to the simulations of R6G dimers in aqueous solution, which were obtained with STD charges and the PME method. The starting configuration is shown in Figure 5.10 where carbethoxyphenyl groups are trans positioned. To facilitate comparison with previous work, [109] we again considered two parts of a 2.5 ns trajectory, separately averaging over a short-time window, up to 0.7 ns, and a long-time window, from 1.5 to 2.5 ns (Table 5.8). We will first discuss the results for the trajectory which, as done before, [109] was started with antiparallel orientation, $\beta = 180°$, of the xantylium moieties. For the short-time window, results for the key structure parameters *M-M* (Figure 5.19a), *M-P*, roll angle α, and twist angle β indeed agree well with previous results [109] and with the results obtained for a P6G dimer (Table 5.6). For the long-time average, one notes a propensity to larger *M-M* distances, (4.41±0.50) Å compared to (3.83±0.26) Å at shorter times, and shorter *M-P* distances, (3.34±0.25) Å compared to (3.62±0.16) Å at shorter times. Yet, corresponding averages at different times are compatible, based on the SD values.

However, this correspondence of short-time and long-time averages does not extend to the torsion angle β (Table 5.8). After 1.5 ns, the R6G dimer exhibits a trend toward a twisted conformation at smaller torsion angles (Figure

5.10b), with β = (135±19)° compared to the short-time average of (157±9)°. From the SD values, both averages are statistically compatible.

Table 5.8 Geometric parameters of a rhodamine 6G dimer, averaged over various time intervals of MD trajectories with different initial structures (β = 120°, 180°). Results obtained from the STD variant of the force field and the PME treatment of the Coulomb interactions as well as those of the previous study (DD/PW) were shown.

	1–700 ps		1501–2500 ps
Charges	STD	DD/PW	STD
M-M, (Å)	3.83±0.26	3.75±0.23	4.41±0.50
M-P, (Å)	3.62±0.16	3.47±0.32	3.34±0.25
Roll α, °	8±6	10±6	15±9
Torsion β, °	157±9		135±19
Torsion β', °	25±10	20±11	56±20

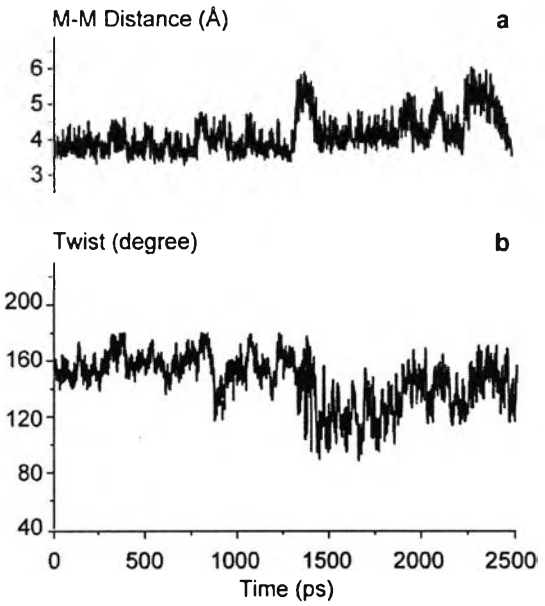

Figure 5.19 *M-M* distance (a) and torsion angle β (b) of R6G see Figure 5.10. Simulation based on the STD charge assignment, treating the Coulomb interaction with the PME technique.

As for the P6G dimer, the results for the torsion angle disagree with those obtained previously. [109] The long-time average values of the alternative

torsion angle β', (56±20)°, describe rather different configurations of R6G dimers than previous results, β' = (20±11)° (Table 5.8). Therefore, torsion angles of the xantene dimers seem to be the structure parameter most sensitive to parameters of the MD simulations, in particular to length of the MD trajectories.

5.3.3 Energy component analysis of monomers and dimers of P6G and R6G

Finally, we turn to an exploration of the driving force responsible for the formation of dimers from two positively charged xantene monomers. This issue deserves further study despite previous discussions.[109,112] As a convincing demonstration of the strength of the driving force to be shown in Figure 5.17 results of an MD simulation on a R6G. It is informative, but it will not be sufficient, to analyze the energy change underlying the dimer formation, based on those trajectories which had previously used when discussing the structure of the dimers (Table 5.9). For the present purpose, the analyzed was separated, both for P6G and R6G dimers, the intra-dimer interactions (dye-dye) from the interaction of a dimer with its aqueous environment (dye-solv, Table 5.9), partitioning these interaction energies further into van der Waals (vdW) and electrostatic (estat) contributions. As reference, the interaction of dye monomers with their solvent was also analyzed, based on separate MD trajectories. The results for the P6G dimer from trajectories with a cutoff-based and a PME treatment of Coulomb interactions were compared in Table 5.9. The analysis of a P6G monomer with results from a trajectory that has been generated with a full Ewald treatment was also complemented (Table 5.9).

Detailed inspection of the P6G data of Table 5.9 reveals three noteworthy results. *(i)* The intra-dimer interaction (dye-dye) is repulsive as electrostatic repulsion substantially exceeds van der Waals attraction, to yield a total repulsive energy of 31 kcal/mol. Therefore, dimerization cannot be discussed without accounting for effects of the solvent environment. [109,112] *(ii)* Including the solvent contributions, the total energy ΔE_{dim} of dimerization is very large, (-77±22) for the PME trajectory and (-56±36) kcal/mol for the cutoff-based trajectory. *(iii)* This "reaction energy" is totally dominated by changes of the electrostatic interaction during dimer formation. The total van der Waals energy of a P6G dimer, intra-dimer

plus dye-solvent interactions, is essentially the same as the van der Waals interaction of two monomers with their environment; the corresponding SD values are notably larger, 6–7 kcal/mol, than the net energy changes, -0.7 kcal/mol (cutoff) to -3.2 kcal/mol (PME) (Table 5.9).

Table 5.9 Energy component analysis[a] of monomers and dimers of P6G and R6G, based on trajectories up to 2.5 ns, generated with the standard variant (STD) of the force field and different treatments of the electrostatic interactions (PME, Ewald, cutoff).

		Dimer			Monomer		
		dye-dye	dye-solv	SE	dye-solv	SE	ΔE_{dim}
P6G							
vdW	Ewald	–	–		-28.2±2.5		–
	PME	-14.0±1.5	-51.0±3.3		-30.9±2.5		-3.2±7.3
	cutoff	-14.1±1.6	-49.0±3.2		-31.2±2.3		-0.7±7.1
estat	Ewald	–	–		-46.0±11.7		–
	PME	45.1±1.5	-159.6±9.2	-110.7±0.2	-47.1±4.9	-28.5±0.1	-74.0±15.9
	cutoff	45.4±1.9	-262.9±23.8		-81.3±10.4		-54.9±36.1
total	Ewald	–	–		-102.7±11.9		–
	PME	31.1±1.5	-321.3±12.7		-106.5±7.5		-77.2±21.7
	cutoff	31.3±1.6	-311.9±23.6		-112.5±10.5		-55.6±35.7
R6G							
vdW	PME	-18.7±2.2	-66.2±4.4		-42.3±2.9		-0.3±9.5
estat	PME	42.1±1.7	-159.4±9.7	-98.6±0.1	-50.1±5.6	-26.5±0.2	-62.7±17.3
total	PME	23.4±1.6	-324.2±10.0		-118.9±6.0		-63.0±17.6

[a] Van der Waals (vdW), electrostatic (estat) and total contributions to the interaction between the two dye moieties of a dimer (dye-dye) as well as a between a solute (dimer, monomer) and its solvent environment (dye-solv). For PME trajectories, the self-energy correction (SE) is also given; see text for details. Binding energy of a dimer:
$\Delta E_{dim} = E_{dimer}(\text{dye-dye}) + E_{dimer}(\text{dye-solv}) + E_{dimer}(\text{SE})$
$- 2\times[E_{monomer}(\text{dye-solv}) + E_{monomer}(\text{SE})]$. All energies in kcal/mol.

The three methods oriented findings would be also like to point out (see Table 5.9). *(i)* Corresponding results on van der Waals energies from both trajectories, PME and cutoff-based, agree very well. *(ii)* The same holds for the intra-dye interaction energies, including their van der Waals and electrostatic components. *(iii)* In contrast, PME and cutoff-based results for the dye-solvent interactions, for both dimers and monomers, exhibit notable discrepancies. As typical result, we mention the electrostatic contribution to the interaction of a P6G dimer with the solvent, which is -

160±9 kcal/mol from the PME-based trajectory, but -263±24 kcal/mol from the cutoff-based trajectory. Besides the large difference of the average values, one should also notice the much smaller SD value of the PME result. We obtained these results by following the standard procedure for evaluating electrostatic interactions with the AMBER package.[122]

The PME results seemingly underestimate the solvation energies of monomers and dimers in a major way compared with corresponding cutoff-based results. However, for a complete analysis of the electrostatic (free) energy of solvation based on an Ewald procedure, one has to add an estimate of the self-energy E_{SE} which accounts for the interaction of a charge with its own periodic images and the neutralizing plasma. [137] For a cubic unit cell of length L (in Å), the self-energy term is $E_{SE} = -943.0\ q^2/L$ kcal/mol where q is the charge of the solvated molecule (in e).[138] In the present study, the shapes of the unit cells are close to cubic; therefore, we estimated the self-energy correction by averaging $L^{-1} \approx V^{-1/3}$ along a trajectory where V is the volume of the unit cell (Table 5.5). Other corrections, *e.g.* for a solvent of low dielectric permittivity [139] or the formation of a solute cavity of non-negligible size (radius R) compared to the unit cell, [140] can be neglected in the present case because $1 << \varepsilon$ and $2\pi R^2/3L^2 << 1$, respectively. With the resulting E_{SE} corrections, PME and cutoff-based electrostatic energy contributions for monomers and dimers of both P6G and R6G agree within their standard deviations (Table 5.9).

We close this discussion of Table 5.9 by comparing results for P6G and R6G. Not unexpectedly, all van der Waals contributions of P6G, intra-dimer and dimer-solvent of the dimer and monomer-solvent, are larger (by absolute value) than the corresponding values for the smaller molecule P6G. However, just as for P6G, the van der Waals interaction of R6G does not provide a net contribution to the dimer formation, (-0.3±9.5) kcal/mol. Again as a consequence of the size of the systems, the electrostatic and the total interaction within a dimer are less repulsive for R6G, *e.g.* 23.4±1.6 kcal/mol for the total energy contribution compared to 31.1±1.5 kcal/mol for P6G. Also for R6G, the self-interaction corrected electrostatic interaction completely dominates the total energy of dimer formation, -63.0±17.6 kcal/mol. Although this average value for R6G is notably smaller than the corresponding PME result for P6G, -77±22 kcal/mol, one cannot draw any conclusion (*e.g.* on the equilibrium constants in

solution), because both values are compatible within the sum of their standard deviations, ~30 kcal/mol.

This analysis of interaction energies yielded dimerization energies comparable to the solvation free energies of ions. Therefore, any direct comparison with experiment based on such an energy analysis [109] is premature without accounting for entropy contributions due to the reorganization of the solvent structure. Entropic effects due to the solute can be largely neglected because structure and internal energy of the xantylium unit are not expected to undergo substantial changes during dimer formation; freezing the "flipping" degrees of freedom of the carbethoxyphenyl moieties would only lead to the loss of a few kcal/mol.

In simulations, solute-solvent entropy effects can directly be addressed based on solute-solvent distribution functions. [141,142] Nevertheless, for a qualitative understanding of these effects as well as for assessing their scaling behavior with the charge and the size of the solute, it is useful to perform some very simplified estimates. One expects that the large favorable changes of the electrostatic energy upon dimerization are balanced by a decrease of the entropy due to a rearrangement of the water molecules in the vicinity of the solute. We estimate for P6G how the number of "bound" water molecules changes during the formation of a dimer.

As above, we focus on heavy atoms and we assume that each such center of a monomer is able to coordinate on average about two solvent molecules if no further steric constraints are active. Then a monomer is estimated to bind $N_{tot}(mon) = 2N$ water molecules, where $N = 22$ for P6G. The value of $N_{tot}(mon) = 44$ is in good agreement with the number of water molecules in the first solvation shell of P6G, estimated along the trajectory by the program AMBER 8 on geometric grounds, [122] 45.1±3.8.

Upon formation of a dimer, the number of immobilized solvent molecules changes for both steric and electrostatic reasons. Extending the preceding steric argument to a dimer, water molecules are expelled from the space "between" the monomers; hence, on first sight, the number of immobilized solvent molecules would be reduced to $N_{tot}(dimer,steric) = 2N_{tot}(mon) - 2N'$ where $N' \approx 14$ is approximately the number of heavy atoms of a xantylium moiety. Again, this estimate of

N_{tot}(dimer,steric) = 60 agrees quite well with the trajectory average of the number of water molecules in the first solvation shell of a P6G dimer, 65.1±4.4. Note that this estimate, alone on steric arguments, would lead to an entropy contribution which would increase (in absolute terms) the free energy driving force for dimerization beyond the already very strong energy contribution discussed above.

However, this reasoning solely on steric grounds neglects the long-range electrostatic effect which can be approximately quantified by the electrostatic potential $\Phi \sim q^2/R$ where R is the effective radius of the solute. Upon dimerization, the charge q of the solute doubles, but the effective radius of the solute increases as well, by about a factor of $2^{1/3}$. Therefore, N_{tot}(dimer,steric) has to be scaled by an electrostatic factor:

$$\lambda = \frac{\Phi_{\text{dimer}}}{\Phi_{\text{monomer}}} = \frac{q^2_{\text{dimer}}}{q^2_{\text{monomer}}} / \frac{R_{\text{dimer}}}{R_{\text{monomer}}} \approx 4/2^{1/3} \sim 3 \tag{5.6}$$

Hence, during formation of a dimer, the number of "bound" water molecules is estimated to increase by

$$\begin{aligned} \Delta N &= \lambda N_{\text{tot}}(\text{dimer,steric}) - 2N_{\text{tot}}(\text{mono}) = (\lambda - 1)2N_{\text{tot}}(\text{mono}) - \lambda 2N' \\ &\approx 8N - 6N' \end{aligned} \tag{5.7}$$

The estimate for P6G dimerization is $\Delta N = 92$. Attributing a change of the free energy by 1 kT due to each of these additionally "bound" solvent molecules, one estimates an entropy induced increase of the free energy upon dimerization by ~55 kcal/mol. Thus, the total free energy change accompanying the dimerization of P6G is significantly smaller (in absolute terms), about -20 kcal/mol, than the total energy of dimerization, -77 kcal/mol (Table 5.9).

This rather qualitative discussion is corroborated by the results of a free energy calculation on the dimerization of P6G via thermodynamic integration. The resulting free energy curve (Figure 5.20) exhibits a minimum near 3.5–3.8 Å which has a ~7 kcal/mol depth, in satisfactory agreement with the above estimate.

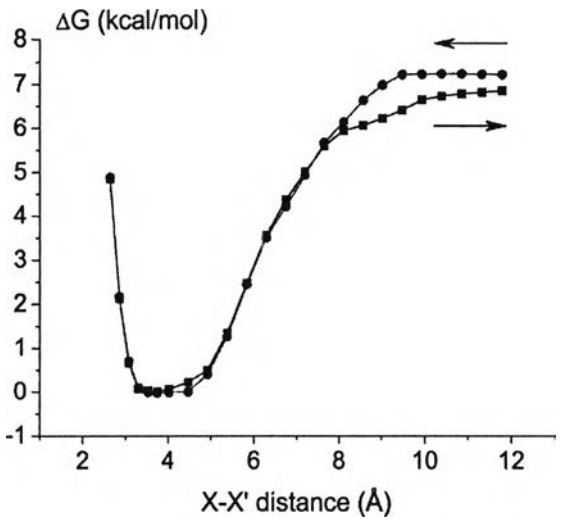

Figure 5.20 Free energy profile of a P6G dimer from thermodynamic integration along the centroid distance *X-X'* in forward and reverse directions; see also Figure 5.9.

One expects a rather similar entropy contribution to the free energy change of forming a R6G dimer because the carbethoxyphenyl moieties should hardly affect the number of "bound" water molecules during dimer formation. In fact, from the trajectory average of the estimated numbers of water molecules in the first solvation shells of R6G monomers and dimers, 60.1±4.3 and 89.7±5.5, respectively, one deduces that about 30 water molecules are "squeezed" from the first solvation shell upon formation of a R6G dimer, very similar to the trajectory estimate of 25 for the formation of a P6G dimer (see above). Thus, given that dimerization energies of R6G and P6G are similar (Table 5.9), the free energy change during the formation of an R6G dimer should be similar. However, the solvent induced entropy contribution to the free energy change does not yield an equally satisfactory estimate as for the P6G dimer, in part because of large uncertainty of the dimerization energies (see the relatively large SD values of ~15 kcal/mol), but most likely because the carbethoxyphenyl sustituent of the xantylium moiety spoils a simple estimate of the Coulomb scaling factor λ. Experimental evidence shows [143–145 that entropy-enthalpy compensation occurs in many chemical and biological processes, resulting in small values of free energies changes.

The driving force of a dimerization reaction often can be expected to be small because the solvent contribution to the dimerization energy scales in very similar fashion as the entropy contribution. We have seen that the total energy of such charged solutes is to a good approximation proportional to the solvation energy, which in turn scales approximately as the electrostatic potential $\Phi \sim q2/R$. As this latter energy dominates the total energy of dimerization, one has for the energy change during dimerization

$$\Delta E_{\text{dim}} \propto \Phi_{\text{dimer}} - 2 \times \Phi_{\text{monomer}} \propto -(\lambda - 2)\frac{q^2_{\text{monomer}}}{R_{\text{monomer}}} \sim \Phi_{\text{monomer}} \tag{5.8}$$

Thus, both the energy and the entropy contributions to the dimerization are expected to scale with q^2/R. Inspection of *Table* 5.9 shows that the estimate of Equation 5.8 holds quite well for P6G and more approximately also for R6G.

5.4 Summary and conclusions

In summary, the results of our MD simulations on P6G and R6G dimers do not fully support the computational findings of the work by Daré-Doyen (DD) *et al.* [109] We have opted for a different computational protocol. Despite considerable effort, we were not able to reconstruct the DD charge assignment which does not comply with the recommended procedure (referred to as STD) for supplementing the chosen force-field AMBER-95.[122] Pertinent minima differ by ~10° in the torsion angle for the rotation within the xantylium dimer. However, we decided to compare for the P6G dimer the results of MD trajectories generated consistently for both charge assignments, STD and DD. In addition, for P6G dimers, we carried out a detailed comparison of an Ewald-type treatment of the Coulomb interaction (PME) with the residue-based cutoff approach chosen previously. [109]

Yet, the largest differences by far between the two computational strategies are due to the fact that the previous discussion [109] of the structure of xantylium dimers was based on too short MD trajectories (1–700 ps) whereas we based interpretation of the structure of dimers on long-time trajectory averages (1501–2500 ps). For P6G

dimers at long times, averages of structural parameters studied agree well between both force field variants, STD and DD. However, according to our results, the average configuration of a P6G dimer for both set of charges exhibits a "twisted" configuration, closer to a parallel arrangement of the xantylium groups, in contrast to an anti-parallel configuration assigned previously.[109] Comparison of long-time (1501–2500 ps) vs. short-time (1–700 ps) parts of the trajectories exhibits a clear propensity for a further rotation away from the anti-parallel configuration. This confirms that short simulation times [109] are not adequate for sampling the phase space of xantylium dimers and sheds some doubt on the possibility to compare short-time MD results with NMR data. We found here that the P6G dimer is actually a rather flexible system regarding the torsion angle.

For the R6G dimer, we performed similar investigations, but restricted them to the STD charge assignment and a PME treatment of Coulomb interactions. Starting from an anti-parallel configuration (torsion angle 180°), we observed a trend towards a twisted conformation, with a torsion angle of ~120° along a trajectory of 2.5 ns. This finding lead us to conclude that even a trajectory of 2.5 ns may not suffice to compare MD findings for R6G dimers with experimental data, in view of the structural complexity introduced by the carbethoxyphenyl substituent of the R6G xantylium moiety. These aspects require further study.

An answer to the question why positively charged xantylium moieties form dimer (or even higher-order aggregates[4]) in aqueous solution was also proposed. A quantification of the straight forward argument which relies on the solvent-induced energy gain as a consequence of the increased charge in the dimer results in dimerization energies of 60–70 kcal/mol. This energy is completely dominated by the electrostatic interaction of the solute with its aqueous environment. We showed that a residue-based cutoff strategy and a PME procedure yield compatible values of the electrostatic energy, if a self-interaction correction is applied to PME results of AMBER8. However, to reach a physically meaningful picture of the dimer formation, one has to turn to a discussion of free energies. For P6G, we proposed an estimate of the solute-solvent entropy change during dimerization, accounting for the reorganization of the solvent in the vicinity of the solute. This entropy related contribution almost cancels the gain in electrostatic energy, as corroborated by a free energy calculation via thermodynamic integration which resulted in driving force for

dimerization of only about -7 kcal/mol. Also these results suggest further studies to arrive at a more complete picture of the structure and dynamics of xantylium dimers. It will be advantageous to base these investigations on free energy calculations to ensure an unbiased sampling of the phase space.